

# Systematic and Statistical Uncertainties in the Non-Gravitational Acceleration of 3I/ATLAS

F. Spada<sup>1</sup>, M. Królikowska<sup>2</sup>, and L. Dones<sup>3</sup>

<sup>1</sup> Università di Catania, Dipartimento di Fisica e Astronomia, Sezione Astrofisica, Via S. Sofia 78, 95123 Catania, Italy

<sup>2</sup> Centrum Badań Kosmicznych Polskiej Akademii Nauk (CBK PAN), Bartycka 18A, 00-716 Warszawa, Poland

<sup>3</sup> Department of Space Studies, Southwest Research Institute, 1301 Walnut St Suite 400, Boulder, CO 80302, USA

## ABSTRACT

We present a detailed analysis of the trajectory of the interstellar comet 3I/ATLAS, focusing on its non-gravitational acceleration (NGA) parameters and their uncertainties. Orbital solutions are computed with models that implement symmetric, time-offset, and asymmetric radial dependence of the outgassing law relative to perihelion. We assess solution robustness through multiple data-selection strategies and comparison with independent determinations. The radial and normal NGA components ( $A_1$  and  $A_3$ ) are broadly consistent across all configurations, whereas the transverse component ( $A_2$ ) is more sensitive to data selection, parameter correlations, and orbital phase coverage. Models with asymmetric radial decay slopes marginally improve the fit, but they also introduce additional degeneracies, contributing to systematic uncertainties. The magnitude of the NGA scaled to 1 au constrains the nucleus size of 3I. While our total acceleration estimates agree well with that of JPL's Small-Body Database solution, inclusion of systematic modeling effects implies a significantly larger uncertainty in the inferred radius of 3I.

**Key words.** Astrometry — Celestial mechanics — Comets: general — Comets: individual: 3I — Methods: numerical

## 1. Introduction

3I/ATLAS is the third interstellar object ever detected passing through the Solar System, identified by the ATLAS survey on a strongly hyperbolic trajectory that is inconsistent with a bound Solar System origin (Denneau et al. 2025; Bolin et al. 2025, Seligman et al. 2025, and references therein). Like its predecessors (1I/'Oumuamua and 2I/Borisov), 3I offers a rare opportunity to directly probe the physical and dynamical properties of small bodies formed around other stars (Moro-Martín 2022; Jewitt & Seligman 2023; Jewitt 2024).

Observations indicate comet-like activity, suggesting that volatile-driven processes play a significant role in its evolution (e.g., Cordiner et al. 2025). Accurately estimating the non-gravitational acceleration (NGA) acting on 3I is therefore essential. Outgassing-driven forces can measurably perturb the trajectory, biasing orbital solutions if neglected or improperly modeled. Reliable constraints on these accelerations are crucial not only for precise orbit determination and ephemeris prediction, but also for inferring intrinsic physical properties such as volatile composition, activity asymmetry, and thermal response. Moreover, robust modeling of non-gravitational effects is necessary to confidently reconstruct the object's incoming asymptotic trajectory, which underpins any attempt to link 3I to a specific Galactic population or stellar birthplace (Hopkins et al. 2025; Taylor & Seligman 2025; Guo et al. 2025; Albrow et al. 2025).

NGA estimates also bear directly on size determinations of the nucleus. To place 3I in context, Jewitt & Seligman

(2023) estimated that 2I had a diameter of  $\sim 0.4$ – $1$  km, assuming a geometric albedo of  $p = 0.1$ . Its dust mass-loss rate at 2 au was reported to be  $\sim 70$  kg s<sup>-1</sup>, although this estimate is likely uncertain at the order-of-magnitude level (Kim et al. 2020). The JPL orbital solution for 2I yields a magnitude of the NGA normalized at 1 au of approximately  $5.3 \cdot 10^{-8}$  au d<sup>-2</sup>, assuming a  $1/r^2$  radial decay of the acceleration, appropriate for outgassing of substances more volatile than water. By contrast, 1I exhibited a NGA approximately five times larger, detectable at the  $\sim 30$ - $\sigma$  level (Michei et al. 2018), but in spite of extensive searches, no cometary activity was detected (e.g., Jewitt et al. 2017; Meech et al. 2017; Ye et al. 2017; Fitzsimmons et al. 2018).

For 3I, reported dust production rates are of order  $\sim 180$  kg s<sup>-1</sup> at 2 au (Jewitt & Luu 2025). The JPL orbital solution for 3I yields a magnitude of the NGA at 1 au of approximately  $5.5 \times 10^{-8}$  au d<sup>-2</sup>, under the assumption that the activity is driven by something more volatile than water, such as CO<sub>2</sub>. Assuming water-driven activity, on the other hand, Ahuja & Ganesh (2025) obtained a NGA of  $\approx 3 \cdot 10^{-6}$  au d<sup>-2</sup>, which seems implausibly large. The similarity in dust production rates and NGA of 2I and 3I therefore suggest that these objects are likely comparable in size, of the order of 1 km in diameter (Forbes & Butler 2026), although a substantially larger early estimate was proposed by Cloete et al. (2025) based on now-outdated upper limits on the NGA.

Independent constraints from surface-brightness limits and sublimation modeling further support a kilometer-scale nucleus for 3I, with the preferred size depending on the dominant volatile and dust grain properties (Jewitt et al. 2025; Cordiner et al. 2025). Most recently, several determi-

Send offprint requests to: F. Spada

nations of the size of 3I, based on different methods, were summarized by Hui et al. (2026), who recommend a diameter of  $\approx 3$  km on the basis of both nucleus extraction techniques and NGA estimates.

The aim of this work is to assess the impact of astrometric uncertainty, modeling, and data selection on the determination of the NGA parameters for 3I, using publicly available astrometric data.

This paper is organized as follows. The observational data used to constrain the trajectory of 3I are described in Section 2. Section 3 outlines the orbit determination approach and the assessment of parameter uncertainties. Results are presented in Section 4 and discussed in Section 5, with conclusions summarized in Section 6.

## 2. Observational data

The astrometric dataset used in this work to constrain the trajectory of 3I consists of optical measurements of its sky position, obtained over 7788 epochs between 2025 May 8 and 2026 Feb 19. The entire dataset is publicly available, and was obtained from the Minor Planet Center (MPC) web interface<sup>1</sup> on 2026 Feb 24.

The astrometric measurements of 3I were acquired by a combination of ground- and space-based facilities. The space-based data include: pre-discovery archival frames from the Transiting Exoplanet Survey Satellite (TESS) in May 2025 (Martinez-Palomera et al. 2025); Hubble Space Telescope (HST) observations obtained during the night of 2025 Jul 21 (Jewitt et al. 2025); target-of-opportunity imaging by the interplanetary spacecraft Psyche and Trace Gas Orbiter (TGO; see Eubanks et al. 2025).

Figure 1 displays the orbit of 3I in the heliocentric ecliptic frame, emphasizing the segment corresponding to the observational arc used for orbit determination in this work (see Section 4.1). 3I reached perihelion on 2025 Oct 29 at a distance of  $q \approx 1.356$  au. The dataset covers a broad range of heliocentric distances, extending to about 6.31 au in the pre-perihelion arc, and to  $\approx 4.05$  au in the post-perihelion arc. With an eccentricity  $e \approx 6.1$ , the trajectory is strongly hyperbolic. Notably, with a  $v_\infty \approx 58$  km s<sup>-1</sup>, 3I is the fastest interstellar object to have been detected in the Solar System to date.

Before the orbit determination analysis, bias corrections following the de-biasing scheme of Eggl et al. (2020) were applied where applicable. Astrometric uncertainties for the ground-based measurements were assigned according to the error model of Vereš et al. (2017); typical uncertainties are of order  $\lesssim 1$  arcsecond, and are generally more conservative than the values estimated by the respective observers and reported in the Astrometry Data Exchange Standard (ADES) format.

Due to the method used to extract astrometric measurement from the TESS pre-discovery images, Martinez-Palomera et al. (2025) estimate their intrinsic uncertainty to be  $\approx 10$  arcseconds, which motivates our conservative choice of 20 arcseconds. For the HST, Psyche, and TGO data points, we adopt uncertainties of 0.25, 2, and 4 arcseconds, respectively (cf. Eubanks et al. 2025).

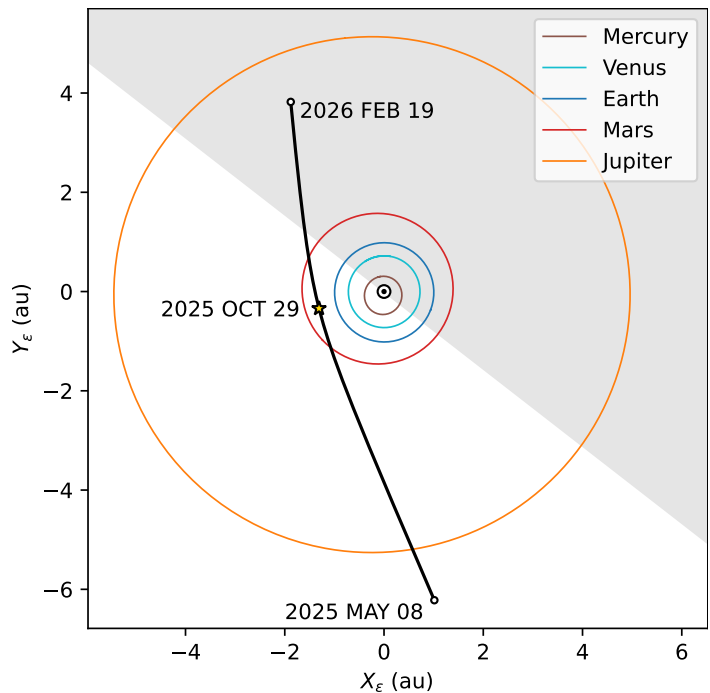


**Fig. 1.** Orbit of 3I in the heliocentric ecliptic reference frame. Perihelion is marked by a yellow star, and the endpoints of the observational arc used for the orbit determination in this study are indicated by open circles. Gray shading denotes the region where  $Z_\epsilon < 0$ . The Sun and the orbits of the major planets through Jupiter are shown for reference.

## 3. Methods

### 3.1. Dynamical model and numerical propagation

Our dynamical model of the trajectory of 3I is based on the numerical integration of the equations of motion expressed in Cartesian coordinates within a heliocentric equatorial reference frame referred to the J2000 equator and equinox. The equations of motion are integrated using the Taylor Adaptive integrator implemented in the *heyoka* package<sup>2</sup> (Biscani & Izzo 2021, 2022).

The total acceleration acting on the body is expressed as the sum of a gravitational and a non-gravitational component. The gravitational part of the acceleration includes the central term from the Sun and perturbations from the major planets, Pluto, and the Moon. The heliocentric positions of the gravitational perturbers are obtained from the analytical theories VSOP2013 (Simon et al. 2013) and ELP2000 (Chapront & Francou 2003) for the planets (including Pluto) and the Moon, respectively, using the implementation of these theories included in *heyoka*. For the gravitational parameters of the perturbers we adopt the numerical values provided by the *heyoka* convenience functions `get_vsop2013_mus`, `get_elp2000_mus`, which reflect the values used in the underlying VSOP2013 and ELP2000 theories. Precision thresholds were set to  $10^{-8}$  for VSOP2013 and  $10^{-6}$  for ELP2000. See Appendix A for an assessment of the numerical accuracy of the integration. The general relativity correction term for solar gravity is also included, according to the post-Newtonian approxima-

<sup>1</sup> <https://data.minorplanetcenter.net/explorer/?tab=Designated&search=3I>

<sup>2</sup> <https://bluescarni.github.io/heyoka.py/index.html>

tion (Damour & Deruelle 1985):

$$\mathbf{a}_{\text{REL}} = \frac{\mu_{\odot}}{c^2 r^3} \left[ \left( \frac{4\mu_{\odot}}{r} - v^2 \right) \mathbf{r} + 4(\mathbf{r} \cdot \mathbf{v}) \mathbf{v} \right], \quad (1)$$

where  $\mu_{\odot}$  is the gravitational parameter of the Sun.

The non-gravitational component of the acceleration is modeled following the Marsden et al. (1973) formalism:

$$\mathbf{a}_{\text{NG}} = g(r) [A_1 \mathbf{e}_R + A_2 \mathbf{e}_T + A_3 \mathbf{e}_N]. \quad (2)$$

In the equation above,  $A_1, A_2, A_3$  are the NGA parameters along the radial, transverse, and normal directions of the standard RTN (radial–transverse–normal) frame, defined by the unit vectors  $\mathbf{e}_R, \mathbf{e}_T, \mathbf{e}_N$ . The vector  $\mathbf{e}_N$  is normal to the instantaneous orbital plane, while  $\mathbf{e}_T$  lies in that plane and is orthogonal to  $\mathbf{e}_R$ , forming a right-handed triad. The function  $g(r)$  describes the heliocentric distance dependence of the outgassing-induced acceleration. Unless otherwise specified, we adopt the original Marsden et al. (1973) parametrization of  $g(r)$ , namely:

$$g(r) = \alpha \left( \frac{r}{r_0} \right)^{-m} \left[ 1 + \left( \frac{r}{r_0} \right)^n \right]^{-k}, \quad (3)$$

with  $\alpha, r_0, m, n, k$  being constant parameters. In all our calculations we adopt  $\alpha = 1$ ,  $r_0 = 1$  au,  $m = 2$ , and  $n = k = 0$ , which correspond to  $g(r) = 1/r^2$ . This choice is based on the assumption that the activity of 3I is driven by something more volatile than  $\text{H}_2\text{O}$ , such as  $\text{CO}_2$  or  $\text{CO}$  (Cordiner et al. 2025). Note that the values of  $\alpha$  and  $r_0$  are such that the magnitude of  $\mathbf{a}_{\text{NG}}$  at 1 au is given by  $A = \sqrt{A_1^2 + A_2^2 + A_3^2}$ .

In this work we consider the following classes of orbital models.

1. Model gr0, implementing purely gravitational dynamics.
2. Model ng1, including NGA symmetric with respect to perihelion (Marsden et al. 1973).
3. Model ng2, in which the NGA features a time offset  $DT$  in the peak outgassing relative to perihelion (Yeomans & Chodas 1989). In this case, the radial dependence function is evaluated at the heliocentric distance corresponding to the delayed time:  $g[r(t + DT)]$ . Since the function  $g(r)$  attains its maximum at perihelion, evaluating it at time  $t + DT$  implies that a positive (negative) value of  $DT$  corresponds to a maximum NGA occurring before (after) perihelion.
4. Model ng3: motivated by observational evidence that the cometary activity of 3I is asymmetric with respect to perihelion in terms of its heliocentric-distance scaling (Hui et al. 2026; Tan et al. 2026), we explore the following alternative prescription for the function  $g(r)$ :

$$g(r) = \alpha \left( \frac{r}{r_0} \right)^{-m} \left[ (1 - S) \left( \frac{r}{r_0} \right)^{+\delta_m} + S \left( \frac{r}{r_0} \right)^{-\delta_m} \right], \quad (4)$$

where, as before,  $\alpha = 1$ ,  $r_0 = 1$  au, and the function  $S$  features by construction a smooth transition occurring at perihelion:

$$S(r) = \frac{1}{2} \left[ 1 + \tanh \left( w \frac{\mathbf{r} \cdot \mathbf{v}}{r v} \right) \right]. \quad (5)$$

The constant parameter  $w$  controls the sharpness of the transition. For numerical convenience, equation (4) introduces an average slope,  $m$ , and a slope difference parameter,  $\delta_m$ . In other words, apart from a short transitional regime close to perihelion, the NGA decreases with heliocentric distance with the effective exponents  $m - \delta_m$  (pre-perihelion) and  $m + \delta_m$  (post-perihelion):

$$g(r) \sim \begin{cases} (r/r_0)^{-m+\delta_m} & \text{before perihelion;} \\ (r/r_0)^{-m-\delta_m} & \text{after perihelion.} \end{cases} \quad (6)$$

### 3.2. Orbit Determination

The orbit of 3I was independently determined from the available astrometric data using a standard batch least-squares orbit determination procedure (e.g., Milani & Gronchi 2010; Farnocchia et al. 2015). The procedure estimates a parameter vector  $\mathbf{x}$  by minimizing the cost function

$$Q(\mathbf{x}) = \boldsymbol{\nu}^T(\mathbf{x}) W \boldsymbol{\nu}(\mathbf{x}), \quad (7)$$

where  $\boldsymbol{\nu}(\mathbf{x})$  is the vector of astrometric (O–C) residuals corresponding to the current estimate of  $\mathbf{x}$ , and  $W$  is the weight matrix, taken as the inverse of the observational covariance matrix. When correlations among observations are neglected,  $W$  is diagonal, with elements given by the inverse squares of the assigned astrometric uncertainties.

The parameter vector  $\mathbf{x}$  always includes the Cartesian heliocentric state vector  $(x, y, z, v_x, v_y, v_z)$  at the reference epoch in the equatorial J2000 frame. In the non-gravitational model ng1,  $\mathbf{x}$  additionally includes the three NGA parameters  $A_1, A_2$ , and  $A_3$  defined in equation (2). In the purely gravitational model gr0, the fit is limited to the state vector components, while in model ng2 the parameter  $DT$  is included as an additional degree of freedom. Similarly, the additional degree of freedom  $\delta_m$  is included in the ng3 orbital fits (see Section 4.3).

After linearization of the residuals with respect to the parameters, the design matrix  $B = \partial \boldsymbol{\nu} / \partial \mathbf{x}$  is introduced, together with the normal matrix  $C = B^T W B$ . The parameter vector is then iteratively updated according to

$$\mathbf{x}^{(k+1)} - \mathbf{x}^{(k)} = -C^{-1} B^T W \boldsymbol{\nu}, \quad (8)$$

where the covariance matrix of the estimated parameters is given by  $\Gamma = C^{-1}$ . Upon convergence,  $\mathbf{x}$  and  $\Gamma$  represent the linearly estimated solution and its associated covariance matrix.

The fitting was carried out using the `orbit_finder` code, a Python-based code specifically designed for orbit determination of small Solar System bodies and publicly available on GitHub (Spada 2024). The `orbit_finder` pipeline implements state-of-the-art prescriptions for bias correction (Eggl et al. 2020), astrometric weighting scheme (Vereš et al. 2017), and iterative outlier rejection (Carpino et al. 2003). In the present work, a development version of the code was employed in which the numerical propagation of the equations of motion is handled by the `heyoka` integrator, as described in Section 3.1. Aside from the substitution of the propagator, all aspects of the batch least-squares estimation procedure are identical to those of the public release, ensuring methodological consistency with previous applications of `orbit_finder` (e.g., Spada 2023, 2025).

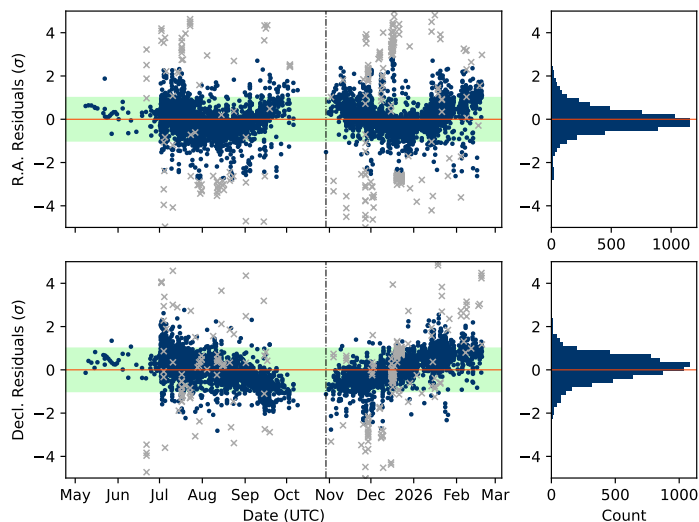


**Fig. 2.** Normalized post-fit residuals of gravity-only orbital fit (model  $gr_0$ ), in right ascension (top panels) and declination (bottom panels). Data points discarded as outliers by the fitting procedure are shown as gray crosses. The dashed vertical line marks the perihelion.

The use of *heyoka* is motivated primarily by computational efficiency and numerical convenience in the present application. For hyperbolic trajectories, over the relatively short observational arc considered here, use of the analytical theories implemented in *heyoka* for the position of the planetary perturbers, even with fairly permissive precision thresholds, incurs no significant loss of accuracy with respect to numerical ephemerides based on more comprehensive dynamical models, such as JPL’s DE440 (see Appendix A for details). On the other hand, the Taylor Adaptive integrator employed by *heyoka* provides performance advantages and built-in support for automatic differentiation. The latter feature, reducing implementation complexity while improving numerical robustness, is especially beneficial for the linearized least-squares estimation implementing different NGA models, such as those discussed in Section 3.1.

## 4. Results

### 4.1. Orbital fits

We performed weighted least-squares fits to the available astrometric observations of 3I, adopting a linearized formulation around a reference fitting epoch. For reference, the full astrometric data set spans the interval from 2025 May 8 to 2026 Feb 19, for a total of 7788 reported epochs. Solar conjunction occurred in October 2025, resulting in a gap in ground-based observations of approximately 20 days, just before the passage through perihelion on October 29.

The fitting epoch, 2025 Sep 1 00:00 TDB, was selected near the midpoint of the observational arc and in proximity to perihelion so as to enhance the sensitivity of the fit to the determination of the NGA parameters, which are the primary quantities of interest in this work.

The observations were weighted and corrected for bias according to the Vereš et al. (2017) and Eggl et al. (2020) prescriptions, respectively. The automated outlier rejection

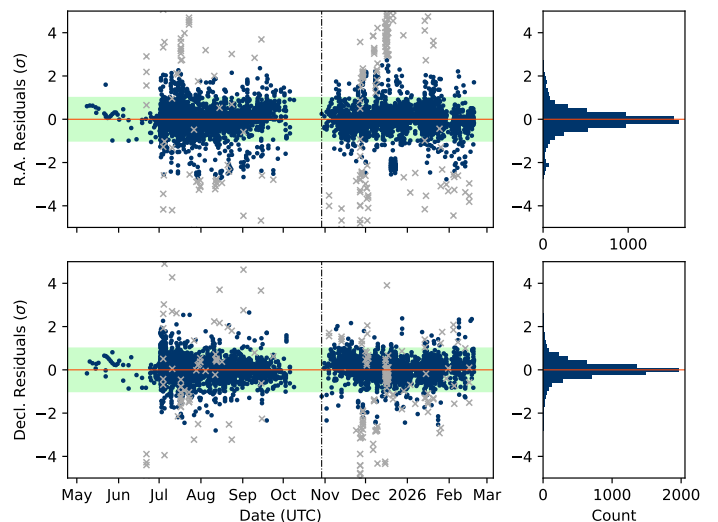


**Fig. 3.** Same as Figure 2, but for dynamical model  $ng_1$ , including NGA according to equation 3 with peak outgassing coinciding with perihelion, applied to the entire dataset.

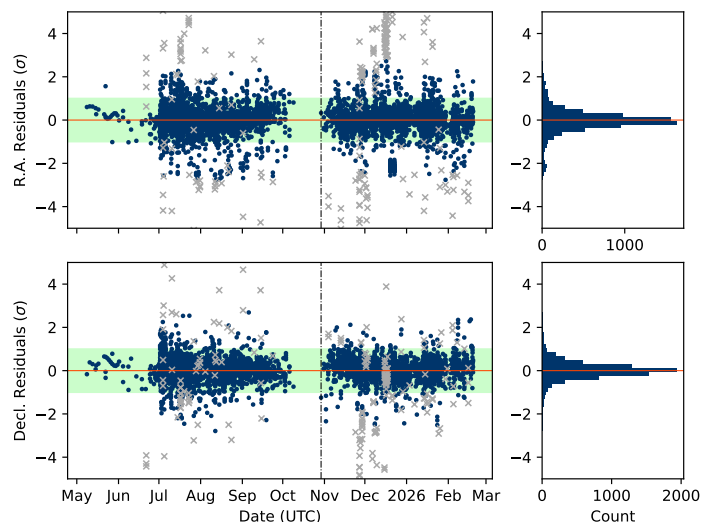


**Fig. 4.** Same as Figures 2 and 3, but for dynamical model  $ng_2$ , including NGA according to equation 3 with peak outgassing offset with respect to perihelion by free parameter  $DT$ , applied to the entire dataset.

procedure described by Carpino et al. (2003), implemented in the *orbit\_finder* pipeline, was applied iteratively during the fitting process.

In this section we discuss seven different orbital solutions: a purely gravitational model ( $gr_0$ ); a symmetric non-gravitational model fitted to the full dataset ( $ng_1$ ); the same symmetric model fitted separately to pre-perihelion observations, with  $A_3$  either estimated ( $ng_{1a}$ ) or fixed to zero ( $ng_{1b}$ ), and to post-perihelion observations, again with  $A_3$  either estimated ( $ng_{1c}$ ) or fixed to zero ( $ng_{1d}$ ); and an asymmetric non-gravitational model, in which the outgassing profile peaks at a time offset from perihelion ( $ng_2$ ). The key figures of these fits are summarized in Table 1.

The normalized post-fit residuals obtained for the gravity-only model  $gr_0$  are shown in Figure 2. Clearly visible long-term trends are present both before and after

**Table 1.** Summary of the orbital solutions obtained with the different dynamical models discussed in the text. For each solution we report the residual RMS, goodness-of-fit statistics, and the estimated NGA parameters, when applicable.

Model	residual RMS (arc sec)	$\chi^2_\nu$	Fitted epochs	$A_1$	$A_2$ ( $10^{-8}$ au d $^{-2}$ )	$A_3$	$A$	$DT$ (d)
gr0	0.669	0.382	7482	N/A	N/A	N/A	N/A	N/A
ng1	0.600	0.260	7578	$3.78 \pm 0.17$	$3.86 \pm 0.17$	$-0.65 \pm 0.02$	$5.44 \pm 0.17$	N/A
ng1a	0.655	0.239	4177	$3.09 \pm 1.64$	$4.48 \pm 2.26$	$-0.90 \pm 0.53$	$5.52 \pm 2.05$	N/A
ng1b	0.656	0.239	4177	$2.87 \pm 1.63$	$4.24 \pm 2.26$	0	$5.12 \pm 2.08$	N/A
ng1c	0.504	0.274	3399	$4.11 \pm 0.66$	$-0.22 \pm 2.86$	$-2.08 \pm 0.27$	$4.62 \pm 0.62$	N/A
ng1d	0.523	0.301	3396	$4.51 \pm 0.66$	$-7.37 \pm 2.64$	0	$8.64 \pm 2.28$	N/A
ng2	0.594	0.259	7578	$3.42 \pm 0.19$	$4.41 \pm 0.17$	$-0.64 \pm 0.02$	$5.62 \pm 0.18$	$6.97 \pm 1.26$

perihelion in the right ascension and declination residuals. These trends are also reflected in the residual distributions, which exhibit peaks offset from zero and somewhat heavy tails. Taken together, these features provide independent evidence for the presence of non-gravitational accelerations affecting the motion of 3I over the observed time span.

The residuals for model ng1 fitted to the complete dataset are shown in Figure 3. In this case, no obvious systematic trends as a function of time are apparent in the residuals. The only notable exception is a cluster of outliers in right ascension located at approximately  $-2.2\sigma$ . The same cluster of measurements exhibiting a systematic bias in right ascension is present in all orbital solutions listed in Table 1, indicating that it is insensitive to the adopted dynamical model. These observations were obtained during the nights of 2025 Dec 19 and 23 by a single observing station (M47). The persistence of this feature across dynamical models, together with the absence of a comparable deviation in declination, suggests that a constant timing offset is the most plausible explanation. A simple estimate based on a weighted average of the ratio between the right ascension residuals and the corresponding apparent right ascension rates yields an offset time  $\Delta t \approx 43$  s. We verified that applying this timing offset to the M47 observations suppresses the right-ascension residual cluster.

The overall RMS of the residuals for the ng1 solution is lower than for the gravity-only solution, and the non-gravitational acceleration parameters are tightly constrained (within  $\approx 5\%$ ). The reduced chi-square for this solution is 0.260, indicating that the adopted observational uncertainties are likely conservative. Overall, the comparison between models gr0 and ng1 provides strong dynamical evidence that a purely gravitational description of the motion is incomplete.

Non-symmetric outgassing with respect to perihelion may affect the determination of the NGA parameters and contribute to their systematic uncertainty. To assess whether such effects are supported by the data, we compare the parameters obtained with model ng1 when restricting the dataset to pre- and post-perihelion observations. Since the orbital fits restricted to the pre- and post-perihelion data yielded large uncertainties on  $A_3$ , the corresponding solutions were repeated with  $A_3 = 0$  held fixed in order to assess the impact on the remaining non-gravitational parameters.

Apart from the larger uncertainties expected from the reduced number of observations, the pre- and post-perihelion fits yield estimates of the transverse NGA parameter,  $A_2$ , that are mutually inconsistent, regardless

of whether  $A_3$  is also included in the fit. On the other hand, the NGA parameters from the pre-perihelion fit remain compatible, within their much larger uncertainty, with those obtained from the full dataset. These results may indicate the presence of non-symmetric outgassing (see, e.g., Królikowska & Dybczyński 2013).

For the ng1c solution, the normal NGA component,  $A_3$ , is significantly larger than the transverse component,  $A_2$ , the latter being consistent with zero within uncertainties. This likely explains why the ng1d solution, which assumes  $A_3 = 0$ , yields a comparatively poorer fit than ng1c. In contrast, the two pre-perihelion fits, ng1a and ng1b, are of comparable quality. We also note that the magnitude of the NGA scaled to 1 au,  $A$ , is consistent across all ng1-type solutions, with the exception of ng1d.

Finally, model ng2, which introduces the delay parameter  $DT$  as an additional degree of freedom, yields a modest improvement in both the residual RMS and the reduced chi-square relative to the symmetric ng1 solution, and comparable post-fit residuals (see Figure 4). The osculating orbital elements and NGA parameters of orbital solutions ng1 and ng2 are given in Table B.1.

In conclusion, while including symmetric NGA in the dynamical model significantly improves the fit relative to a purely gravitational model, the discrepancy between the pre- and post-perihelion solutions suggests that a symmetric formulation may be incomplete. We note that the inferred NGA, particularly  $A_1$  and  $A_2$ , may be subject to significant systematic variations if non-symmetric outgassing effects are present. The issue of the dynamical effects of an asymmetry in the cometary activity of 3I is explored further using a different approach in Section 4.3.

#### 4.2. Uncertainty characterization for the NGA parameters

Table 2 summarizes the nominal values of the NGA parameters and their uncertainties for the dynamical model ng1, estimated using three independent methods:

1. Uncertainties derived from the covariance matrix of the linearized orbital fit.
2. Markov-Chain Monte Carlo (MCMC) sampling of the posterior probability distribution.
3. Jackknife analysis with two different data removal strategies.

The vector magnitude of the NGA scaled to 1 au is also included in Table 2. Overall, the nominal values are broadly consistent across all methods.

**Table 2.** Estimated NGA parameters with their uncertainties for orbital solution ng1. For the Jackknife entries, median values with their minimum–maximum ranges are reported (wnd and stn refer to the sliding window and observing station removal strategies (see Section 4.2).

method	$A_1$	$A_2$	$A_3$	$A$
	$10^{-8} \text{ au d}^{-2}$			
Orbital Fit (ng1)	$3.778 \pm 0.175$	$3.860 \pm 0.165$	$-0.651 \pm 0.017$	$5.441 \pm 0.169$
MCMC sampling	$4.072^{+0.172}_{-0.176}$	$3.341^{+0.163}_{-0.162}$	$-0.685^{+0.017}_{-0.017}$	$5.311 \pm 0.170$
Jackknife (wnd)	3.790 (3.299, 4.052)	3.958 (3.474, 4.430)	-0.654 (-0.691, -0.647)	5.425 (5.238, 5.949)
Jackknife (stn)	3.763 (2.737, 3.932)	3.885 (3.518, 4.249)	-0.652 (-0.669, -0.650)	5.442 (5.099, 5.452)

The orbit determination procedure provides an estimate of the uncertainty of the parameters along with their nominal values. These uncertainties are encoded in the covariance matrix  $\Gamma = C^{-1}$  obtained from the inversion of the normal matrix (see Section 3.2), under the assumptions of the linearized least-squares framework, which include local linearity of the observation equations (that is, the relationships between the state vector and the theoretically predicted astrometric positions) and Gaussian observational errors. Their accuracy may therefore be limited by non-linear effects, parameter correlations, and departures from Gaussianity (e.g., Milani & Gronchi 2010).

We employ a MCMC sampling to characterize the posterior distribution of the parameters around the nominal solution obtained from the least-squares orbital fit. In this context, the MCMC sampling is useful to assess the extent of parameter correlations and non-Gaussianity of their distribution. We define the likelihood function consistently with that assumed in the linearized orbital fit (see, e.g., Farnocchia et al. 2015):

$$\mathcal{L}(\mathbf{x}) = \frac{1}{\sqrt{(2\pi)^n \det W^{-1}}} \exp\left(-\frac{1}{2}\boldsymbol{\nu}^T W \boldsymbol{\nu}\right), \quad (9)$$

where  $n$  is the number of independent observational constraints, that is, in our case, twice the number of epochs at which both right ascension and declination have been measured. In the equation above, the dependence of the likelihood on the parameter vector  $\mathbf{x}$  through the residuals vector  $\boldsymbol{\nu}$  has been written down explicitly.

We included non-informative priors on the components of the Cartesian state vector, while we imposed the uniform priors  $|A_i| \leq 50 \cdot 10^{-8} \text{ au d}^{-2}$ , with  $i = 1, 2, 3$  on the NGA parameters. The sampling was performed using all available observations, including those rejected by the outlier detection algorithm in the linearized orbit determination procedure, in order to obtain a conservative estimate of the uncertainties. As a tradeoff, we can expect broader posterior distributions and/or moderately biased median values compared with the results of the orbital fit. For each parameter, the median of the posterior distribution was adopted as the nominal value. The lower uncertainty was defined as the difference between the median and the 16th percentile, and the upper uncertainty as the difference between the 84th percentile and the median.

We ran the MCMC sampling with 36 walkers, each advanced for 6,000 steps using the affine-invariant ensemble sampler `emcee` (Foreman-Mackey et al. 2013). The first 1,000 steps of each walker were discarded as burn-in, and the chains were thinned by retaining every 10th sample, resulting in 18,000 samples for each parameter. Visual inspection indicates that the resulting chains are well-mixed

and the posteriors smooth and unimodal. The MCMC posterior distributions are shown in Figure 5 in a standard corner plot, with the nominal values of the orbital fit overlaid along with their 1- and 2- $\sigma$  contours.

Considering the differences discussed above, the orbital fit and the MCMC sampling are in agreement at the expected level. The posteriors are well approximated by Gaussian distributions. The moderate shift in the NGA parameters likely arises because the MCMC analysis includes data points rejected as outliers in the linearized fit. Direct tests (not shown here) indicate that MCMC sampling applied to the same dataset as the converged linearized fit yields posterior distributions whose means and variances are consistent with those of the multivariate Gaussian defined by the covariance matrix from the orbital fit. Among the NGA parameters,  $A_1$  and  $A_2$  exhibit the largest discrepancy and show the strongest correlations with other components of the state vector, particularly  $v_x$  ( $A_1$ ) and  $v_y$  and  $v_z$  ( $A_2$ ).

The correlations between the NGA parameters and the components of the state vector can be understood in terms of the orbital geometry of 3I. In a linearized orbit determination framework, correlations arise when velocity perturbations induced by a given NGA component project along directions similar to those produced by perturbations in the corresponding initial velocity components. For 3I, near perihelion, when NGA is maximum, the radial direction aligns closely with the negative  $x$ -axis, while the transverse direction projects primarily onto the  $y$ - $z$  plane (see Figure 1). Consequently, correlations are expected between  $A_1$  and  $v_x$ , and between  $A_2$  and  $v_y$  and  $v_z$ , as observed in Figure 5. By contrast, the normal direction is orthogonal to the orbital plane and induces cross-track motion that cannot be efficiently absorbed by in-plane velocity adjustments. As a result,  $A_3$  is generally only weakly correlated with the Cartesian state vector.

To assess the sensitivity of the orbital solution to specific subsets of the data, we also performed a jackknife analysis using two complementary strategies. In the first, we excluded observations within a sliding window of approximately equal size in terms of mean anomaly, repeating the orbital fit for each censored dataset (six runs in total). In the second, we excluded observations from six selected observing stations, again repeating the fit for each case. Specifically, in the latter case, these exclusions comprised two of the most represented stations in the current dataset (W68, ATLAS Chile, Rio Hurtado, and T05, ATLAS-HKO, Haleakala), observing station M47 (see discussion in Section 4.1), the TESS data, the HST data, and the combined dataset obtained with Psyche and TGO.

Figure 6 provides a visual illustration of the two jackknife strategies, showing how the sliding-window and

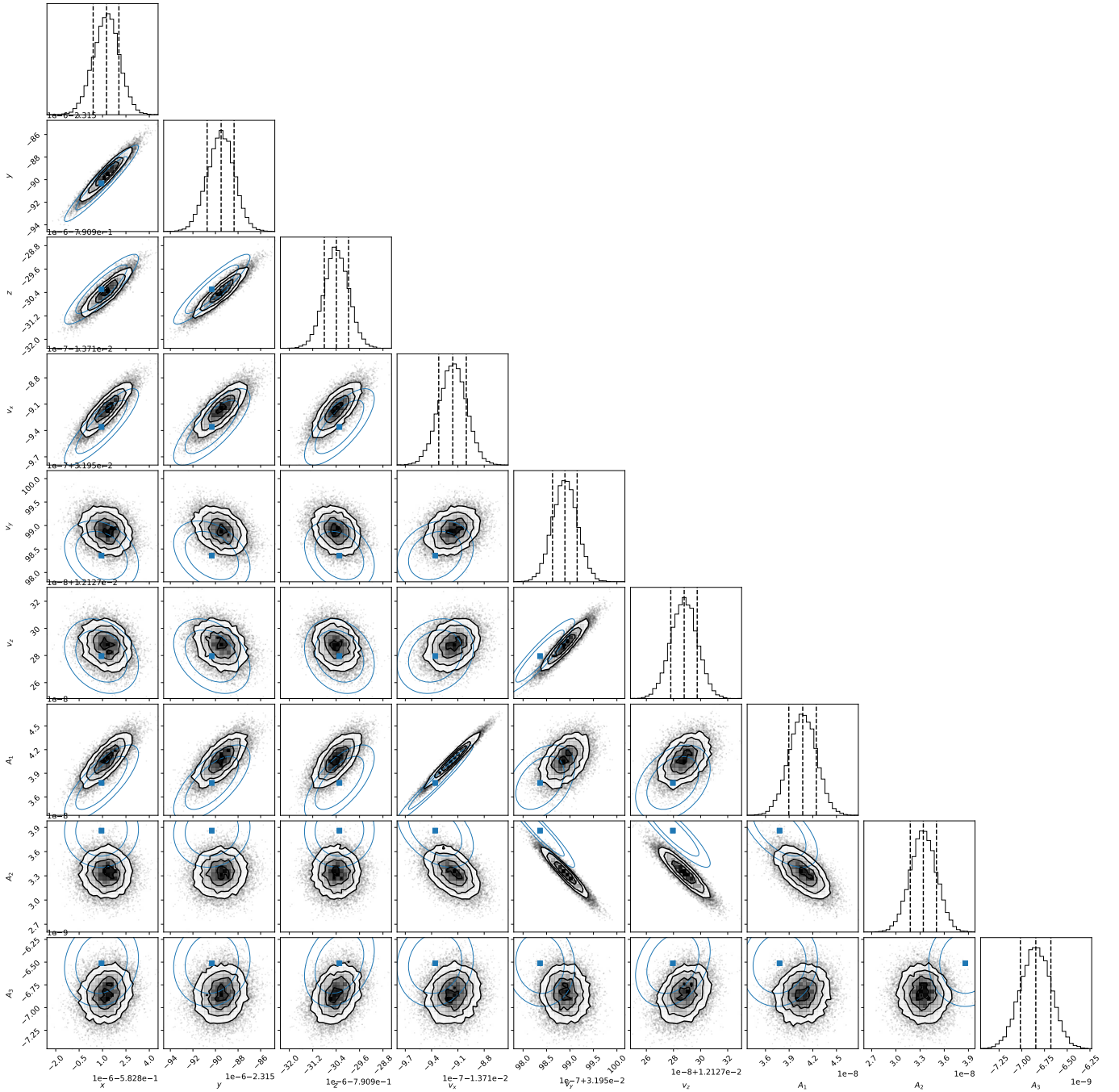


**Fig. 5.** Sampled posterior distribution for parameters of model ng1. Sampled parameters vector comprises the components of the state vector in the heliocentric equatorial frame and the NGA parameters. The nominal values of the parameters from the orbital fit along with their 1- and 2- $\sigma$  contour lines are also plotted in the off-diagonal panels (blue squares and blue lines, respectively).

station-based removals affect different portions of the observational arc. The gap in the observations in October 2025 corresponds to the period when 3I was in solar conjunction as seen from Earth.

Because the number of observations removed in each trial is not constant under either strategy, the standard jackknife expressions for estimating nominal values and uncertainties (e.g., Hogg et al. 2010) are not applicable. Instead, for each parameter we extract the median and the minimum–maximum range across the ensemble of jackknife

trials, which we use as a descriptive measure of the robustness of the solution rather than as a formal uncertainty estimate. These figures are reported in Table 2. This approach suffices to probe the sensitivity of the nominal values of the parameters and of their uncertainties to specific observations or groups of observations.

In the sliding-window removal strategy (left column panels in Figure 6), nominal values remain close to the orbital fit and MCMC results, but the range of variability is substantially larger than implied by the statistical un-

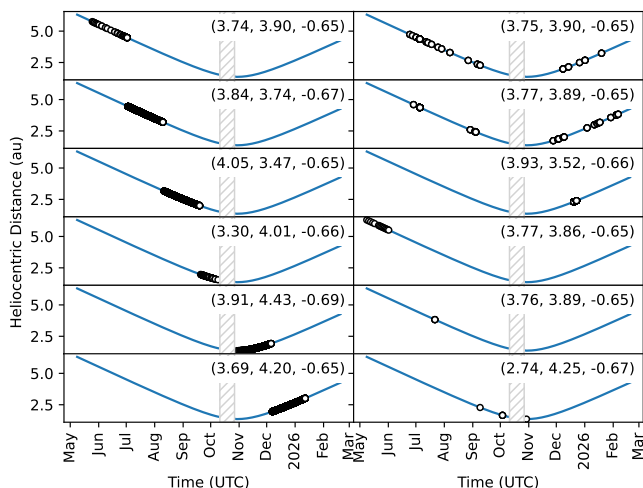


**Fig. 6.** Visual illustration of the jackknife data-removal strategies. The left column shows the sliding-window approach, while the right column shows the removal by observing station. In each panel, the removed data are indicated by open black circles, while the solar conjunction interval is marked by gray hatching. The estimated NGA parameters for each case are also reported, in units of  $10^{-8}$  au d $^{-2}$ .

certainties. This indicates varying sensitivity of the fit to observations at different orbital phases, such as near or far from perihelion. This behavior is analogous to the extreme differences observed when the ng1 model is fitted to only pre- or post-perihelion data, which was discussed in the previous section (see also Table 1).

In the observing-station removal strategy, illustrated in the right column panels of Figure 6, most of the fits to the censored data produce only minor changes in the NGA parameters, indicating that none of these subsets dominates the solution. A notable exception occurs when the Psyche and TGO data points are removed, resulting in a relatively large change in  $A_1$  and moderate changes in  $A_2$  and  $A_3$  (bottom right panel). This marked dependence on a very small subset of data points was already reported by Eubanks et al. (2025). The large impact of the deep-space spacecraft data points highlights the importance of observations obtained from heliocentric vantage points and observing times that are inaccessible to ground-based or near-Earth orbit observing facilities.

In summary, the nominal NGA parameters are stable across methods, and the uncertainties derived from MCMC and jackknife analyses provide a realistic assessment of parameter precision. The transverse component  $A_2$  exhibits the greatest sensitivity to the dataset and fitting strategy.

#### 4.3. Exploring the asymmetry of the NGA radial dependence

Observational evidence indicates that the cometary activity of 3I was significantly asymmetric with respect to the perihelion in terms of the water production rate (Tan et al. 2026), as well as the activity index (Hui et al. 2026). Although other interpretations are possible, this observed behavior may point to an asymmetry in outgassing, and consequently in the radial decay of the NGA when moving away from the time of its peak. To test this possibility, we repeated our least-squares orbital fit of 3I with model ng3,

implementing NGA scaling with the heliocentric distance according to equation (4). In this fit, the parameters  $m$  and  $\delta_m$  control the average exponent, and the difference of the effective pre- and post-perihelion exponents, respectively.

When fitting model ng3, the parameters  $m$ ,  $\delta_m$ , and the overall scale factor of the NGA parameters are strongly correlated, leading to degeneracies in both least-squares and MCMC approaches. Specifically, larger values of  $m$  require a larger overall NGA magnitude,  $A$ , to fit the same observations, due to the steeper radial decay of the acceleration with heliocentric distance. This quasi-degeneracy can only be effectively broken if observational data sampling a wide range of heliocentric distances are available. Our preliminary tests showed that both the orbital fit and the MCMC sampling encounter convergence issues, the former due to ill-conditioning of the normal matrix, and the latter due to a nearly flat likelihood surface in parameter space, which could lead to poorly constrained or even misleading parameter estimates.

For these reasons, we do not attempt to estimate all parameters of model ng3 simultaneously, but rather sample a range of values for the average exponent  $m$ , fitting the remaining parameters for each choice. Our results are summarized in Table 3. As expected, varying  $m$  leads to systematic changes in the best-fitting values of  $\delta_m$  and of the NGA coefficients. The slope difference parameter  $\delta_m$  is positive in all cases, corresponding to a steepening of the NGA radial decay law when moving from pre- to post-perihelion.

The systematic increase of the NGA parameters with the average slope parameter  $m$  reflects the fact that, as  $m$  increases, the corresponding function  $g(r)$  becomes more strongly peaked. Consequently, the magnitude of the NGA must increase in order to produce approximately the same integrated effect over the observed trajectory.

In spite of the significant variations in the fitted parameters, the quality of the fits is not very sensitive to  $m$ , with only a slight preference for values between 3 and 4. The goodness-of-fit metrics are also very close to those of the ng1 and ng2 models discussed above. Overall, the available data are therefore not very sensitive to the details of the radial dependence of the NGA. As stated above, this behavior can be understood by noting that the observations span a limited range of heliocentric distances. Within this interval, different combinations of the parameters can produce nearly identical integrated non-gravitational effects along the trajectory. The effect is illustrated in Figure 7, which shows the magnitude of the NGA as a function of heliocentric distance for the fits reported in Table 3.

All the fits discussed so far were performed with  $w = 20$ . Analogous calculations for  $w = 2$  (not shown here), corresponding to an extended transitional regime between the pre- and post-perihelion phases, show that this parameter has only a modest impact on the results.

In Figure 7, the magnitude of the NGA for our ng3-type models is compared with that obtained for the ng2 model discussed in Section 4.1. The time evolution of  $A \cdot g(r)$  for the ng3 model with  $m = 2$  is broadly similar to that of model ng2. Likewise, the corresponding NGA parameters inferred from the ng2 and ng3 ( $m = 2$ ) orbital fits are, consistently, very close. Moreover, all ng3 fits shown in the figure converge to values of  $m$  and  $\delta_m$  that yield an NGA peak offset comparable to that of the ng2 solution. This suggests that, over the observed arc, variations in slope asymmetry can mimic an effective shift in the peak of the NGA, and

**Table 3.** Parameters of the orbital fits implementing the asymmetric radial decay law (4). The effective pre- and post-perihelion exponents are calculated as  $m_{\text{pre}} = m - \delta_m$  and  $m_{\text{post}} = m + \delta_m$ .

$m$	res. RMS (arc sec)	$\chi_v^2$	$m_{\text{pre}}$	$m_{\text{post}}$	$A_1$	$A_2$ ( $10^{-8}$ au d $^{-2}$ )	$A_3$	$A$
2.0	0.595	0.259	$1.73 \pm 0.06$	$2.27 \pm 0.06$	$3.21 \pm 0.22$	$4.38 \pm 0.17$	$-0.63 \pm 0.02$	$5.46 \pm 0.18$
3.0	0.594	0.260	$2.55 \pm 0.07$	$3.45 \pm 0.07$	$5.73 \pm 0.36$	$5.65 \pm 0.23$	$-1.02 \pm 0.03$	$8.11 \pm 0.30$
4.0	0.593	0.260	$3.47 \pm 0.10$	$4.53 \pm 0.10$	$9.73 \pm 0.58$	$7.54 \pm 0.34$	$-1.61 \pm 0.05$	$12.41 \pm 0.50$
5.0	0.595	0.261	$4.44 \pm 0.12$	$5.56 \pm 0.12$	$15.65 \pm 0.91$	$10.25 \pm 0.53$	$-2.47 \pm 0.08$	$18.87 \pm 0.81$

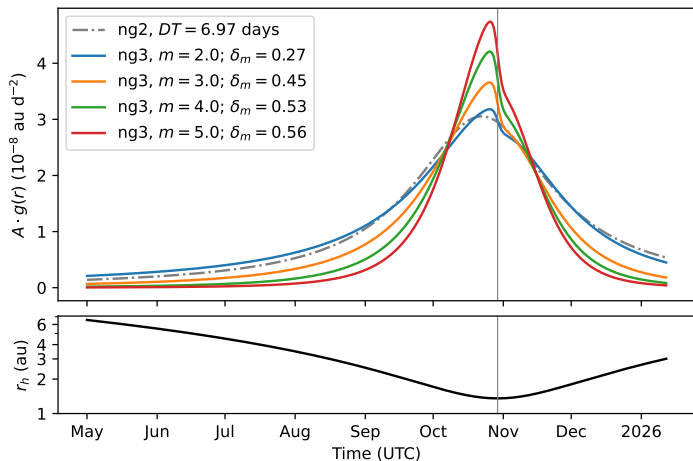


**Fig. 7.** Magnitude of the NGA as a function of time for the fits reported in Table 3. The bottom panel shows the corresponding variation of the heliocentric distance.

vice versa, resulting in a partial degeneracy between the two parameterizations.

The additional degree of freedom, and accompanying degeneracy, arising from  $\delta_m$  (or  $DT$ ) introduces a further systematic source of uncertainty on the NGA coefficients and on the total acceleration amplitude  $A$ . Even restricting our considerations to the values of  $m$  in the range 3–4, this uncertainty amounts to a factor of  $\approx 1.5$ . It would therefore be very valuable to obtain an independent estimate of  $m$  from the observations. In this respect, we note that the activity index of 3I across perihelion was reported as  $3.8 \pm 0.3$  pre-perihelion (Jewitt & Luu 2025) and  $4.5 \pm 0.3$  post-perihelion (Hui et al. 2026). These values are roughly consistent with the pre- and post-perihelion slopes of our ng3 model with  $m = 4$ , which also provides the best-quality fit. On the other hand, the reported water production rates, even extracted from the same dataset, are currently controversial (see Combi et al. 2025; Tan et al. 2026).

It should be emphasized that, since both ng2 and ng3 parameterizations project onto essentially the same observable feature in the data, namely an offset of the peak NGA with respect to perihelion, interpreting differences in the pre- and post-perihelion slopes as physically distinct from a simple peak offset may be unwarranted.

## 5. Discussion

Our estimates of the NGA coefficients can be directly compared with the orbital solution for 3I available in JPL’s Small-Body Database (SBDB) (JPL 2026). At the time of

writing (late February 2026), an ng2-type solution, in which  $g(r) = 1/r^2$  is assumed, is available on the SBDB. Its best-fitting NGA parameters are  $5.320 \pm 0.122$ ,  $1.148 \pm 0.214$ ,  $-0.6854 \pm 0.0178$  (all in units of  $10^{-8}$  au d $^{-2}$ ), and  $9.479 \pm 1.426$ , obtained for the fitting epoch 2026 Feb 19.0 TDB. Comparing these values with those reported in Table 1 for our ng2 solution, we see moderate, or even small, discrepancies in the parameters  $A_1$ ,  $A_3$ , and  $DT$ , whereas the difference in  $A_2$  is substantial. Given the similar treatment of the NGA, the discrepancies are most plausibly attributable to differences in the pre-processing of the observations and in the adopted error model. In particular, the JPL solution quoted above is based on data at 782 epochs, reflecting a significant vetting and/or pre-processing of the public dataset currently available for 3I.

Additional determinations of the NGA parameters were presented by Cloete et al. (2025) and Ahuja & Ganesh (2025, 2026). However, these analyses relied on more limited datasets, notably lacking post-perihelion observations, and employed NGA models that differ significantly from ours. For these reasons, we do not attempt a direct comparison with those results.

Eubanks et al. (2025) reported orbital fits for 3I that include NGA effects. The solutions labeled “E+P+TGO (3 d.f.)” and “E+P+TGO (4 d.f.)” in their Table 1 correspond most closely to our models ng1 and ng2, respectively. In both cases, significant quantitative and qualitative differences are evident. In particular, their four-degree-of-freedom solution yields negative best-fitting values of  $A_1$  and  $DT$ , which have physical interpretations at odds with those of our ng2 solution: a negative radial NGA component is not readily explained within the conventional sublimation-driven framework, while a negative  $DT$  implies a peak outgassing delayed, rather than anticipated, with respect to perihelion. Again, these discrepancies are likely due to differences in the observational dataset and in the adopted uncertainty model.

In summary, among the previously published NGA determinations for 3I, the solution provided by JPL’s SBDB is overall the most consistent with ours. A notable difference between the JPL ng2 solution and ours concerns the relative amplitudes of the NGA parameters: in the JPL case,  $A_2$  is approximately a factor of five smaller than  $A_1$ , whereas in our solution  $A_2 \approx A_1$ . A physical argument supporting the plausibility of radial and transverse accelerations of comparable magnitude is provided by recent high-resolution imaging of 3I. Observations reported by Serracart et al. (2026) reveal collimated, high-latitude jets in the inner coma that display a periodic wobble consistent with nucleus rotation. This morphology indicates localized and anisotropic outgassing rather than uniform sublimation. Furthermore, post-perihelion imaging with the HST

confirms the persistence of multiple mini-jets, modulated by a  $\approx 7.1$  hr rotational period and consistent with a spin-axis orientation within  $\approx 20^\circ$  of the sunward direction (Scarmato & Loeb 2026). Such a configuration naturally favors strongly directional gas and dust emission, capable of generating a transverse acceleration component comparable in magnitude to the radial one.

In this work, we identified and quantified the main sources of uncertainty affecting the determination of the NGA parameters for 3I. Our preferred orbital solutions are obtained using the two most common approaches to modeling the NGA: a radial dependence symmetric with respect to perihelion (model ng1), and an asymmetric dependence implemented as a freely adjustable time offset in the peak outgassing (model ng2). We also obtain a comparably satisfactory fit with an alternative prescription that assumes an asymmetric radial decay of the outgassing rate away from its maximum.

When the impact of different data-removal strategies is also considered, a clear pattern emerges. The normal acceleration coefficient  $A_3$  is the most stable across models and datasets, followed by the radial coefficient  $A_1$ . In contrast, the transverse coefficient  $A_2$  is the most sensitive to the details of the fitting procedure. This behavior, which is also evident from comparison with other independent determinations discussed above, differs from the more common case of small bodies on bound (elliptical) orbits. For elliptical orbits,  $A_2$  is typically more robustly determined than  $A_1$ , since the latter suffers from a strong degeneracy with the semi-major axis through its connection with the orbital period (Farnocchia et al. 2015). Such a degeneracy obviously does not arise for hyperbolic orbits.

Accurate determination of the NGA parameters is essential for estimating the nucleus size of 3I. All other quantities being equal, the radius scales with the magnitude of the NGA normalized at 1 au approximately as  $\frac{\delta R}{R} \sim \frac{1}{3} \frac{\delta A}{A}$  (see equation 10 of Hui et al. 2020). Our estimate of  $A$  for our ng2 solution is fully compatible with that of the latest JPL solution ( $5.619 \pm 0.18$  vs  $5.485 \pm 0.13$ , all values in units of  $10^{-8}$  au d $^{-2}$ ). If the additional systematic effects on  $A$  associated with our asymmetric radial decay models ng3 are included (see Section 4.3), however, the corresponding relative uncertainty in the radius can be as large as  $\approx 50\%$ .

## 6. Conclusions

We presented an analysis of the trajectory of the interstellar comet 3I, with particular emphasis on the determination of its non-gravitational acceleration parameters and on a systematic assessment of their uncertainties using multiple data selections and modeling approaches.

We find that the radial and normal components,  $A_1$  and  $A_3$ , are stable and consistently determined across all tested configurations, showing moderate discrepancies with respect to the latest JPL orbital solution. In contrast, the transverse component  $A_2$  is sensitive to data selection, parameter correlations, and orbital phase coverage, and is therefore the least robustly constrained coefficient. A significant discrepancy is also found between our estimate of  $A_2$  and that reported by JPL.

Motivated by observational indications of asymmetric activity, we explored an alternative parameterization of the NGA in which the radial decay slope differs before and after

perihelion. These models do not yield a statistically significant improvement in the quality of the fit relative to the standard prescriptions (symmetric, and with asymmetry parameterized as a time offset of peak outgassing). However, they introduce a degeneracy between the radial decay exponents and the NGA coefficients, which contributes an additional systematic component to the overall uncertainty in the total acceleration. These systematic effects can propagate to the total non-gravitational acceleration scaled to 1 au and, in turn, significantly affect the estimate of the nucleus size of 3I.

*Acknowledgements.* This research has made use of positional data of 3I provided by the International Astronomical Union's Minor Planet Center.

## References

- Ahuja, G. & Ganesh, S. 2025, ApJ, 995, 1, L13. doi:10.3847/2041-8213/ae21cf
- Ahuja, G. & Ganesh, S. 2026, Research Notes of the American Astronomical Society, 10, 1, 19. doi:10.3847/2515-5172/ae3c09
- Albrow, L., Bannister, M. T., Forbes, J. C., et al. 2025, arXiv:2512.04700. doi:10.48550/arXiv.2512.04700
- Biscani, F. & Izzo, D. 2021, MNRAS, 504, 2, 2614. doi:10.1093/mnras/stab1032
- Biscani, F. & Izzo, D. 2022, MNRAS, 513, 4, 4833. doi:10.1093/mnras/stac1092
- Bolin, B. T., Belyakov, M., Fremling, C., et al. 2025, MNRAS, 542, 1, L139. doi:10.1093/mnras/rlaf078
- Carpino, M., Milani, A., & Chesley, S. R. 2003, Icarus, 166, 2, 248. doi:10.1016/S0019-1035(03)00051-4
- Chapront, J. & Francou, G. 2003, A&A, 404, 735. doi:10.1051/0004-6361:20030529
- Cloete, R., Loeb, A., & Vereš, P. 2025, arXiv:2509.21408. doi:10.48550/arXiv.2509.21408
- Combi, M. R., Mäkinen, T., Bertaux, J.-L., et al. 2025, arXiv:2512.22354. doi:10.48550/arXiv.2512.22354
- Cordiner, M. A., Roth, N. X., Kelley, M. S. P., et al. 2025, ApJ, 991, 2, L43. doi:10.3847/2041-8213/ae0647
- Damour, T. & Deruelle, N. 1985, Annales de L'Institut Henri Poincaré Section (A) Physique Theorique, 43, 1, 107.
- Denneau, L., Siverd, R., Tonry, J., et al. 2025, Minor Planet Electronic Circulars, 2025-N12. doi:10.48377/MPEC/2025-N12
- Egg, S., Farnocchia, D., Chamberlin, A. B., et al. 2020, Icarus, 339, 113596
- Eubanks, T. M., Hibberd, A., Bills, B. G., et al. 2025, Research Notes of the American Astronomical Society, 9, 12, 329. doi:10.3847/2515-5172/ae2915
- Farnocchia, D., Chesley, S. R., Milani, A., et al. 2015, Asteroids IV, 815. doi:10.2458/azu\_uapress\_9780816532131-ch041
- Fitzsimmons, A., Snodgrass, C., Rozitis, B., et al. 2018, Nature Astronomy, 2, 133. doi:10.1038/s41550-017-0361-4
- Forbes, J. C. & Butler, H. 2026, Research Notes of the American Astronomical Society, 10, 1, 12. doi:10.3847/2515-5172/ae3747
- Foreman-Mackey, D., Hogg, D. W., Lang, D., et al. 2013, PASP, 125, 306.
- Guo, Y., Zhang, L., Feng, F., et al. 2025, AJ, 170, 6, 362. doi:10.3847/1538-3881/ae1833
- Hogg, D. W., Bovy, J., & Lang, D. 2010, arXiv:1008.4686. doi:10.48550/arXiv.1008.4686
- Holman, M. J., Akmal, A., Farnocchia, D., et al. 2023, PSJ, 4, 4, 69. doi:10.3847/PSJ/acc9a9
- Hopkins, M. J., Dorsey, R. C., Forbes, J. C., et al. 2025, ApJ, 990, 2, L30. doi:10.3847/2041-8213/adfbf4
- Hui, M.-T., Ye, Q.-Z., Föhrling, D., et al. 2020, AJ, 160, 2, 92. doi:10.3847/1538-3881/ab9df8
- Hui, M.-T., Jewitt, D., Mutchler, M. J., et al. 2026, arXiv:2601.21569. doi:10.48550/arXiv.2601.21569
- Jewitt, D., Luu, J., Rajagopal, J., et al. 2017, ApJ, 850, 2, L36. doi:10.3847/2041-8213/aa9b2f
- Jewitt, D. 2024, arXiv:2407.06475. doi:10.48550/arXiv.2407.06475
- Jewitt, D., Hui, M.-T., Mutchler, M., et al. 2025, ApJ, 990, 1, L2. doi:10.3847/2041-8213/adf8d8

- Jewitt, D. & Luu, J. 2025, *ApJ*, 994, 1, L3. doi:10.3847/2041-8213/ae1832
- Jewitt, D. & Seligman, D. Z. 2023, *ARA&A*, 61, 197. doi:10.1146/annurev-astro-071221-054221
- Jet Propulsion Laboratory. 2026, *JPL Small-Body Database: 3I/ATLAS*, [https://ssd.jpl.nasa.gov/tools/sbdb\\_lookup.html#/?sstr=3I](https://ssd.jpl.nasa.gov/tools/sbdb_lookup.html#/?sstr=3I), accessed 2026 Feb 24
- Kim, Y., Jewitt, D., Mutchler, M., et al. 2020, *ApJ*, 895, 2, L34. doi:10.3847/2041-8213/ab9228
- Królikowska, M. & Dones, L. 2023, *A&A*, 678, A113. doi:10.1051/0004-6361/202347178
- Królikowska, M. & Dybczyński, P. A. 2013, *MNRAS*, 435, 1, 440. doi:10.1093/mnras/stt1313
- Martinez-Palomera, J., Tuson, A., Hedges, C., et al. 2025, *ApJ*, 994, 2, L51. doi:10.3847/2041-8213/ae1f91
- Marsden, B. G., Sekanina, Z., & Yeomans, D. K. 1973, *AJ*, 78, 211. doi:10.1086/111402
- Meech, K. J., Weryk, R., Micheli, M., et al. 2017, *Nature*, 552, 7685, 378. doi:10.1038/nature25020
- Micheli, M., Farnocchia, D., Meech, K. J., et al. 2018, *Nature*, 559, 223. doi:10.1038/s41586-018-0254-4
- Milani, A. and Gronchi, G., 2010. *Theory of orbit determination*. Cambridge University Press.
- Moro-Martín, A. 2022, arXiv:2205.04277. doi:10.48550/arXiv.2205.04277
- Park, R. S., Folkner, W. M., Williams, J. G., et al. 2021, *AJ*, 161, 3, 105. doi:10.3847/1538-3881/abd414
- Scarmato, T., & Loeb, A. 2026, arXiv:2602.18512. doi:10.48550/arXiv.2602.18512
- Seligman, D. Z., Micheli, M., Farnocchia, D., et al. 2025, *ApJ*, 989, 2, L36. doi:10.3847/2041-8213/adf49a
- Serra-Ricart, M., Licandro, J., & Alarcon, M. R. 2026, *A&A*, 705, L3. doi:10.1051/0004-6361/202558072
- Simon, J.-L., Francou, G., Fienga, A., et al. 2013, *A&A*, 557, A49. doi:10.1051/0004-6361/201321843
- Spada, F. 2023, arXiv:2304.06964.
- Spada 2024, *orbit\_finder*, GitHub repository, [https://github.com/federico-spada/orbit\\_finder](https://github.com/federico-spada/orbit_finder)
- Spada, F. 2025, *Research Notes of the American Astronomical Society*, 9, 3, 58. doi:10.3847/2515-5172/adbf9a
- Tan, H., Yan, X., & Li, J.-Y. 2026, arXiv:2601.15443. doi:10.48550/arXiv.2601.15443
- Taylor, A. G. & Seligman, D. Z. 2025, *ApJ*, 990, 1, L14. doi:10.3847/2041-8213/adfa28
- Vereš, P., Farnocchia, D., Chesley, S. R., et al. 2017, *Icarus*, 296, 139.
- Ye, Q.-Z., Zhang, Q., Kelley, M. S. P., et al. 2017, *ApJ*, 851, 1, L5. doi:10.3847/2041-8213/aa9a34
- Yeomans, D. K. & Chodas, P. W. 1989, *AJ*, 98, 1083. doi:10.1086/115198

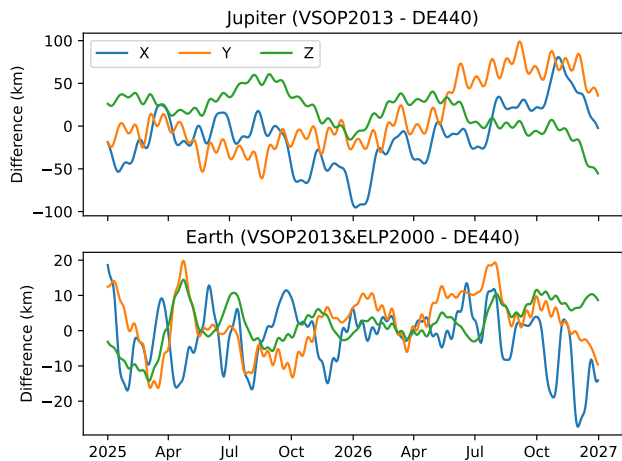


**Fig. A.1.** Difference in heliocentric planetary positions (in the ICRS frame) between the predictions of the analytical theories VSOP2013 and ELP2000, as implemented in *heyoka*, and the DE440 JPL ephemerides. Numerical precision thresholds were set to  $10^{-8}$  for VSOP2013 and  $10^{-6}$  for ELP2000.

## Appendix A: Validating the propagation

The *heyoka*-based propagator described in Section 3.1 accounts for planetary perturbations using the analytical theories VSOP2013 and ELP2000 to compute the positions of the planets (including Pluto) and of the Moon, respectively.

When the complete series are retained, the accuracy relative to high-precision numerical integrations is roughly at the sub-meter level for the inner planets (with the exception of Mars) and at the kilometer level for the outer planets (except Pluto) for VSOP2013, while ELP2000 achieves centimeter-level accuracy. Truncation of small-amplitude terms reduces computational cost at the expense of precision. In the *heyoka* implementation, optional input parameters define a numerical threshold: terms with coefficients below this value are omitted from the series.

To quantify the impact of the truncation thresholds, we computed the differences in heliocentric ICRS positions of Jupiter and the Earth predicted by the analytical theories and by the DE440 JPL ephemerides (Park et al. 2021). The results are shown in Figure A.1 for truncation thresholds of  $10^{-8}$  (VSOP2013) and  $10^{-6}$  (ELP2000), which are the values adopted in our calculations throughout the paper. Since VSOP2013 provides only the heliocentric position of the Earth–Moon barycenter, the position of the Earth is obtained by combining VSOP2013 with ELP2000. For comparison, increasing the thresholds to  $10^{-7}$  (VSOP2013) and  $10^{-5}$  (ELP2000) increases the differences with respect to DE440 by a factor of  $\lesssim 10$  over the same time interval shown in Figure A.1.

We further validated the *heyoka*-based propagator against a propagator built on the ASSIST package (Holman et al. 2023), using comparable perturbation settings (options PLANETS, GR\_EIH, and NON\_GRAVITATIONAL enabled; all others disabled). The comparison is shown in Figure A.2. In all computations, the truncation thresholds were set to  $10^{-8}$  (VSOP2013) and  $10^{-6}$  (ELP2000).

Both propagators are tested on our nominal ng1 solution, with initial conditions defined at the reference epoch

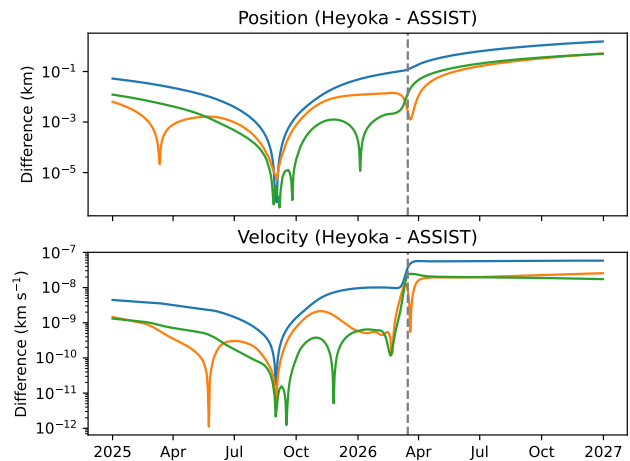


**Fig. A.2.** Difference in position and velocity for the ng1 orbital solution obtained with the *heyoka*- vs ASSIST-based propagators. The vertical grey line marks the time of the expected close encounter with Jupiter.

2025 Sep 1 00:00 TDB. Over the interval from January 2025 to mid-March 2026, the two integrations agree to within  $\lesssim 0.1$  km in position and  $\lesssim 10^{-8}$  km s $^{-1}$  in velocity. After the encounter with Jupiter on 2026 March 16, the differences increase substantially, as expected from the strong dynamical sensitivity of the trajectory to this event.

Additional numerical experiments indicate that even relatively loose truncation thresholds, such as  $10^{-6}$  (VSOP2013) and  $10^{-4}$  (ELP2000), have only a minor effect on the NGA parameters derived in our orbital fits, at the level of less than 1%.

## Appendix B: Osculating elements of our orbital fits

Table B.1 reports the osculating heliocentric elements for the orbital solution ng1, ng2 (see Section 4.1) and ng3 (with  $m = 4$ , see Section 4.3). All the orbital elements in the table are referred to the ecliptic plane and evaluated at the fit epoch 2025 Sep 1 00:00 TDB. The tabulated values are intended to provide a reproducible numerical representation of the orbital solutions, enabling direct comparison among the different fits presented in this work, as well as comparison with independent determinations available in the literature.

These orbital fits incorporate different prescriptions of the NGA: maximum amplitude at perihelion (ng1); peak offset with respect to perihelion through a free parameter (ng2); asymmetric activity decay law about perihelion (ng3).

All elements correspond to osculating quantities at the stated epoch. In particular, the mean anomaly is defined consistently with the adopted dynamical model and reference frame. Care should therefore be exercised when comparing these values with solutions obtained under different modeling assumptions (e.g., planetary ephemerides, relativistic corrections, or non-gravitational force parameterizations), as such differences may result in small but non-negligible offsets even at the same epoch.

**Table B.1.** Heliocentric osculating orbital elements, referred to the ecliptic plane, for the fits implementing various NGA prescriptions discussed in Section 4.1 and 4.3. All solutions are referred to the epoch 2025 Sep 1 00:00 TDB. Rows from top to bottom report: eccentricity, semi-major axis, perihelion distance, inclination, longitude of the ascending node, argument of perihelion, and mean anomaly at epoch. The NGA parameters reported in the last five rows are defined in Section 3.1.

	ng1	ng2	ng3 ( $m = 4$ )
$e$	$6.13933588 \pm 1.247 \cdot 10^{-5}$	$6.13925639 \pm 1.953 \cdot 10^{-5}$	$6.13929378 \pm 1.850 \cdot 10^{-5}$
$a$ (au)	$-0.26393225 \pm 4.309 \cdot 10^{-7}$	$-0.26393498 \pm 6.531 \cdot 10^{-7}$	$-0.26393255 \pm 5.866 \cdot 10^{-7}$
$q$ (au)	$1.35643647 \pm 2.091 \cdot 10^{-6}$	$1.35642954 \pm 2.551 \cdot 10^{-6}$	$1.35642692 \pm 2.576 \cdot 10^{-6}$
$I$ (deg)	$175.1131 \pm 2.060 \cdot 10^{-5}$	$175.1131 \pm 2.106 \cdot 10^{-5}$	$175.1131 \pm 2.169 \cdot 10^{-5}$
$\Omega$ (deg)	$322.1569 \pm 3.400 \cdot 10^{-4}$	$322.1571 \pm 4.047 \cdot 10^{-4}$	$322.1572 \pm 3.892 \cdot 10^{-4}$
$\omega$ (deg)	$128.0096 \pm 3.152 \cdot 10^{-4}$	$128.0098 \pm 3.943 \cdot 10^{-4}$	$128.0101 \pm 3.783 \cdot 10^{-4}$
$M_0$ (deg)	$-425.1024 \pm 9.025 \cdot 10^{-4}$	$-425.0967 \pm 1.359 \cdot 10^{-3}$	$-425.1023 \pm 1.217 \cdot 10^{-3}$
$A_1$ (au d $^{-2}$ )	$3.7781 \cdot 10^{-8} \pm 1.750 \cdot 10^{-9}$	$3.4191 \cdot 10^{-8} \pm 1.860 \cdot 10^{-9}$	$9.7298 \cdot 10^{-8} \pm 5.820 \cdot 10^{-9}$
$A_2$ (au d $^{-2}$ )	$3.8605 \cdot 10^{-8} \pm 1.651 \cdot 10^{-9}$	$4.4125 \cdot 10^{-8} \pm 1.718 \cdot 10^{-9}$	$7.5398 \cdot 10^{-8} \pm 3.407 \cdot 10^{-9}$
$A_3$ (au d $^{-2}$ )	$-6.5121 \cdot 10^{-9} \pm 1.727 \cdot 10^{-10}$	$-6.4215 \cdot 10^{-9} \pm 1.727 \cdot 10^{-10}$	$-1.6055 \cdot 10^{-8} \pm 4.854 \cdot 10^{-10}$
$DT$ (d)	N/A	$6.968 \pm 1.263$	N/A
$\delta_m$	N/A	N/A	$0.532 \pm 0.095$